Reaction Mechanism of Manganese Superoxide Dismutase Studied by Combined Quantum and Molecular Mechanical Calculations and Multiconfigurational Methods.

Srnec, Martin; Aquilante, Francesco; Ryde, Ulf; Rulíšek, Lubomír

Published in:
The Journal of Physical Chemistry Part B

DOI:
10.1021/jp810247u

2009

Document Version:
Peer reviewed version (aka post-print)

Reaction Mechanism of Manganese Superoxide Dismutase Studied by Combined Quantum and Molecular Mechanical Calculations and Multiconfigurational Methods (LR: ??)

Martin Srnec,[§] *Francesco Aquilante,*[‖] *Ulf Ryde,*[‡] *and Lubomír Rulíšek*[§*]

Gilead Sciences & IOCB Research Center, Institute of Organic Chemistry and Biochemistry, Academy of Sciences of the Czech Republic, Flemingovo nám. 2, 166 10 Praha 6, Czech Republic, Department of Theoretical Chemistry, Lund University, Chemical Center, P.O. Box 124, S–221 00 Lund, Sweden, Department of Physical Chemistry, University of Geneva, 30 Quai Ernest Ansermet, CH-1211 Geneva, Switzerland

E-mail: rulisek@uochb.cas.cz

RECEIVED DATE

TITLE RUNNING HEAD Reaction Mechanism of Manganese Superoxide Dismutase

---

[§] Institute of Organic Chemistry and Biochemistry AS CR, Prague, Czech Republic

[‖] Department of Physical Chemistry, University of Geneva, Geneva, Switzerland

[‡] Dept. Theoretical Chemistry, Lund University, Lund, Sweden

[*] Corresponding Author. Tel.(Fax): +420-220-183-263(578)

ABSTRACT. Manganese superoxide dismutases (MnSODs) are enzymes that convert two molecules of the poisonous superoxide radical into molecular oxygen and hydrogen peroxide. The manganese ion cycles between the Mn^{2+} and Mn^{3+} oxidation states during the reaction and accomplishes its enzymatic action in two half-cycles (corresponding to oxidation and reduction of $O_2^{\bullet-}$). Despite many experimental and theoretical studies dealing with SODs, including quantum chemical active-site-model studies of several variants of reaction mechanisms, several details of MnSODs enzymatic action are still not clear. In this study, we model and compare four reaction pathways (associative, dissociative, and two second-sphere) in the protein environment using the QM/MM approach (combined quantum and molecular mechanics calculations) at the density functional theory level. The results are complemented by CASSCF/CASPT2/MM single-point energy calculations for the most plausible models to properly account for the multireference character of the various spin multiplets. The results indicate that the oxidation of $O_2^{\bullet-}$ to O_2 most likely occurs by an associative mechanism following a two-state (quartet–octet) reaction profile. The barrier height is estimated to be less than 25 kJ.mol^{-1}. On the other hand, the conversion of $O_2^{\bullet-}$ to H_2O_2 probably takes place by a second-sphere mechanism, that is, without a direct coordination of superoxide radical to manganese centre. The reaction pathway involves the conical intersection of two quintet states, giving rise to an activation barrier of ~60 kJ.mol^{-1}. The calculations also indicate that associative mechanism can be a competitive pathway in the second half-reaction, with an overall activation barrier only slightly higher than that of the second sphere mechanism. Activation barriers along the proposed reaction pathways are in reasonable good agreement with the experimentally observed reaction rates of SODs ($k_{cat} \approx 10^4 - 10^5$ s^{-1}). **Xxx This corresponds to activation energies of 45–50 kJ.**

1. Introduction

The superoxide dismutases (SODs) catalyze the seemingly simple disproportionation reaction

$$2\ O_2^{\bullet -} + 2\ H^+ \rightarrow O_2 + H_2O_2 \qquad (1),$$

in which two molecules of the poisonous superoxide radical are converted to molecular oxygen and hydrogen peroxide. In this way, the oxidative damage, caused by radicals derived from water-induced superoxide dismutation, such as the very reactive $OH^{\bullet}$ radical, is prevented.[1]

As a part of the protective system, SODs are found in all aerobic organisms. There are at least three unrelated families of SODs: the structurally homologous mononuclear iron and manganese SODs,[2,3] the binuclear copper–zinc SODs,[4] and the mononuclear nickel SOD.[5] They differ in terms of specific function. The CuZnSODs are found in eukaryotic cytoplasm and are probably important for the clean-up of oxidative pollution from the immune system.[4,6] FeSODs are found in the periplasmic space of bacteria and in chloroplasts of plants, a few protists, and possibly in other eukaryotes, providing resistance to environmental or immunological oxidative stress.[2,7] MnSODs are found in bacteria and in the mitochondria of eukaryotes, where most of the O_2 is reduced. They are believed to protect DNA from endogenous oxidative stress.[3,8]

In the MnSODs, the active site is buried in the enzyme. However, the entrance/exit channel for the substrate (superoxide) is well defined. Moreover, this channel is mostly flanked by positively charged amino acids, which attracts the negatively charged superoxide ion to the neighborhood of the active site (Figure 1).

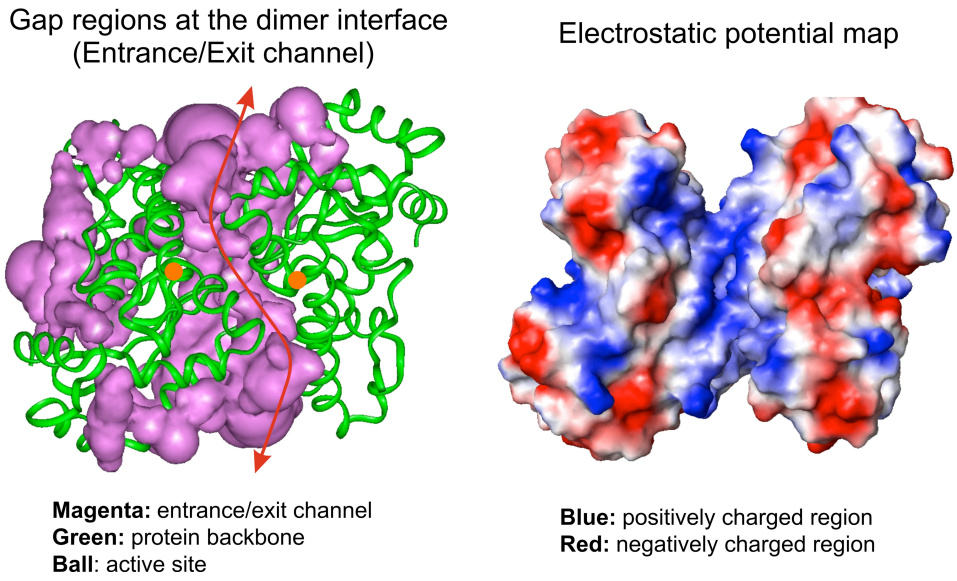

Figure 1. The overall view of MnSOD including (a) gap regions at the dimer interface giving rise to entrance/exit channels to the active site (manganese ions are depicted in orange), (b) electrostatic potential map. **(to MS: to change Magenta: entrance/exit channels to 'gap regions at the dimer interface')** xxx What do you mean by "gap regions"? Is it the interface between the two subunits or what? What is actually colored in magenta (and how)? Is this figure really needed?

In the MnSODs and FeSODs, the mechanism of $O_2^{\bullet-}$ dismutation involves two half-reactions with the metal ion (M) cycling between the +III and +II formal oxidation states.[9] As revealed by crystal structures,[3] the active site consists of the metal ion, bound to one aspartate residue (Asp) in an equatorial position and three histidine (His) residues binding via their $N^{\varepsilon 2}$ atoms to the metal ion (one axial and two equatorial). A solvent molecule completes the trigonal bipyramidal structure, occupying the axial position opposite to one of the His ligands. Atomic resolution (0.9 Å) crystal structures of Mn^{II} and Mn^{III}SODs have recently been presented.[10] Although these are in fact mutants (Tyr174Phe), they have enabled, together with a subsequent quantum refinement study (i.e., a combined QM/MM and X-ray refinement),[11] a clear assignment of the protonation states of the metal-bound water molecule. It brought direct evidence to the consensual belief that this molecule is a hydroxide ion in the oxidized state, but a

water molecule in the reduced state,[3,12,13] yielding the two half-reactions:

$$M^{III}SOD_{OH} + O_2^{\bullet-} + H^+ \rightarrow M^{II}SOD_{H_2O} + O_2 \quad (2)$$

$$M^{II}SOD_{H_2O} + O_2^{\bullet-} + H^+ \rightarrow M^{III}SOD_{OH} + H_2O_2 \quad (3),$$

where the second proton is likely to be shuttled via a conserved[14,15] tyrosine residue (Tyr34 in MnSOD from *Escherichia coli*), which is within 6 Å of the metal ion and has a pK_a of ~9, corresponding to the pH where the enzyme looses catalytic activity.[2] A near-by glutamine residue (Gln146) is also supposed to be involved in the necessary proton shuttles.[16,17] However, it should be noted that the Tyr34Phe mutant retains at least 40% of the wild-type activity.[14,18,19]

The details of this mechanism are of great biochemical importance because the SODs are implied in oxidative-stress induced disorders. Many diseases, including cancer and amyotrophic lateral sclerosis (ALS), can be caused by the radical damage of biological molecules, and the interest in therapeutic mimics is growing.[20,21,22] The reaction is also appealing owing to its speed; SODs work at rates close to the diffusion limit, e.g. $k_{cat}/K_m \approx 2 \times 10^9$ $M^{-1}s^{-1}$ for human MnSOD.[23]

Superoxide can in principle bind to the metal center in SOD in three different ways: by replacing one of the normal ligands, most likely the solvent molecule (a dissociative mechanism), by increasing the coordination number to six (an associative mechanism), or without forming a direct bond to the metal ion (a second-sphere mechanism). A six-coordinate, octahedral intermediate has been observed in both Fe^{III}SOD and Mn^{III}SOD crystal structures with N_3^-.[24] Likewise, spectroscopic studies indicate that the NO adduct to Fe^{II}SOD is six-coordinate.[25] This has been taken as evidences that the associative mechanism is normally preferred. However, anions like N_3^- and F^- do not bind directly to the reduced metal, which has been interpreted in favor of a second-sphere binding of the substrate in this oxidation state.[2,26,27] A putative second-sphere binding site has been identified 5–7.5 Å from the metal ion, in the

vicinity of the conserved Tyr34 and His30 residues.[2,11] The lower estimate (5 Å) comes from molecular dynamics (MD) simulations,[11] whereas the upper estimate was derived from indirect experimental evidence based on the available crystal structure.[2] Last but not least, there is no guarantee that these substrate analogues behave the same way as the substrate, the superoxide radical-anion.

Theoretical endeavors aimed at understanding the enzymatic action of these key enzymes have begun to emerge. Rationalization of electronic structure and electronic absorption spectra by density functional theory (DFT) calculations has been applied as a supplement to spectroscopy.[28] Likewise, Brunold and coworkers have combined spectroscopic techniques with DFT and semiempirical calculations for the study of native, mutant, and metal-substituted Fe and MnSODs.[15,29,30,31,32] They have shown that second-sphere residues are involved in the substrate binding and selectivity, the tuning of the reduction potential, and proton transfer in the active sites. Finally, Noodleman and coworkers have studied the reduction potentials of Fe and MnSOD and their coupling to the deprotonation of the metal-bound solvent molecule.[33,34] Again, they found important influence of second-sphere residues.

A systematic computational study of all possible intermediates expected to be involved in the reaction cycle of Fe- and MnSODs have recently been published.[35] There, the most of conceivable bonding arrangements were analyzed for a small first-sphere model of active site. It was concluded that the first half-reaction – conversion of $O_2^{\bullet -}$ radical into $^3O_2$ molecule – is likely to proceed via the associative mechanism, with all the reaction steps exergonic. For the second half-reaction – conversion of $O_2^{\bullet -}$ radical into peroxide molecule – the situation is less clear. However, it was suggested that the second-sphere complexes are preferred at least for some reaction intermediates. This half-reaction also involved one step that was endergonic by 2–14 $kJ.mol^{-1}$.

In the present study, we utilize the results of this extensive study and model the complete reaction cycle in the native protein environment with the QM/MM approach. This provides a set of consistent data that would enable us to distinguish between the three types of mechanisms for the two half-cycles, i.e., dissociative, associative, and second sphere, and clarify the remaining uncertainties in the reaction

mechanism of this highly interesting class of enzymes. Since many of the low- or intermediate-spin states are not properly described by single-reference methods, such as DFT, the calculated energies are complemented by multireference calculations (complete active space self-consistent field, CASSCF, and complete active space second-order perturbation theory, CASPT2). In addition, qualitative arguments, based on the Marcus theory of electron transfer are used to evaluate the probability of the second-sphere reaction mechanisms.

2. Methods

2.1. Combined Quantum Mechanical and Molecular Mechanical Calculations. All QM/MM calculations were carried out using the COMQUM program.[36,37] In the current version, it combines Turbomole 5.7[38] for the QM part with AMBER 8[39] and the Cornell force field[40] for the MM part. In this approach, the protein and solvent are divided into three subsystems: The QM region (system 1) contains the most interesting atoms and is relaxed by the QM/MM forces. System 2 consists of all residues within 8 Å of any atom in system 1 and is relaxed by a full MM minimization in each step of the QM/MM geometry optimization. Finally, system 3 contains the remaining part of the protein and surrounding solvent molecules and is kept fixed at the original (crystallographic) coordinates. In the QM calculations, the QM system is represented by a wave function, whereas all the other atoms are represented by an array of partial point charges, one for each atom, taken from Amber libraries. Thereby, the polarization of the QM system by the surroundings is included in a self-consistent manner. In the MM calculations for the QM/MM forces and energies, all atoms are represented by the Amber force field.

When there is a bond between systems 1 and 2 (a junction), the quantum region is truncated by hydrogen atoms, the positions of which are linearly related to the corresponding carbon atoms in the full system (the hydrogen link-atom approach).[36,41] In order to avoid overpolarisation of the quantum system, point charges on atoms in MM region bound to junction atoms are set to zero and the remaining charges of the truncated amino acid are adjusted to keep the fragment neutral. The actual charges used for all atoms can be found in the sample PDB file in the supplementary material (last column).

The total energy is calculated as:

$$E_{tot} = E_{QM} + E_{MM123} - E_{MM1} \quad (4)$$

Here, E_{QM} is the QM energy of the quantum system truncated by the hydrogen atoms, which includes the interaction of quantum system with the surrounding point charges (MM part), but excluding the self-energy of the point charges. E_{MM1} is the MM energy of the quantum system, still truncated by hydrogen atoms, but without any electrostatic interactions. Finally, E_{MM123} is the classical energy of all atoms with normal atoms at the junctions and with the charges of the quantum system set to zero (to avoid double-counting of the electrostatic interactions). By using this approach, which is similar to the one used in the ONIOM method,[42] errors caused by the truncation of the quantum system should cancel out. The calculated forces are the negative gradient of this energy, but owing to the differing junctions in the various calculations, they have to be corrected using the chain rule.

2.2. The protein setup. All calculations reported in this work are based on the atomic-resolution (0.9 Å) crystal structure of MnSOD from *Escherichia coli* in the oxidized state (protein data bank accession code 1IX9).[10] The protein is homodimer. In our QM/MM protocol, the reaction was assumed to take place only in the active site of one monomer, whereas the second site was assumed to be a spectator in the Mn^{3+}-OH^- state (arbitrarily chosen and conserved throughout).

Hydrogen atoms were added by the *leap* module of the Amber software, assuming that all Asp and Glu residues are negatively charged and all Lys and Arg residues are positively charged. The protonation status of the His residues were determined by a study of the hydrogen-bond pattern, the surroundings, and the solvent exposure of each residue: His17, 26, 81, and 171 was assumed to be protonated on the $N^{\delta 1}$ atom, whereas the remaining histidine residues (His27, 30, 31, and 78) were assumed to be protonated on the $N^{\varepsilon 2}$ atom (the crystal structures were determined at pH 8.5). This choice made the protein neutral for the Mn^{3+}–OH^- and Mn^{2+}–H_2O states of the active site.

The protein was solvated in a sphere of explicit TIP3P water molecules with a radius of 39 Å. Approximately 4280 water molecules were added, yielding ~21910 atoms in the simulations. The added water molecules were kept inside the sphere by a force constant of 6.3 $kJ.mol^{-1}.Å^{-2}$. The positions of all hydrogen atoms and added water molecules were first minimized and then equilibrated for 300 ps using a simulated annealing protocol (i.e., heating the system to 370 K and cooling it slowly down to 0 K), keeping all heavy atoms at the original positions.

Charges for the Mn ion and its ligands in the MM region (i.e., the active site in the spectator monomer) were taken from the QM calculations (without Gln146). The QM electrostatic potential was calculated in 10 000 random points up to 8 Å from the molecule. The charges were then fitted to these potentials, using a Boltzmann weight for points close to the active-site model. In the fit, it was ensured that the total charge and dipole moment was exactly reproduced, whereas the fit was restrained to reproduce also the quadrupole and octupole moment (the CHELP-BOW procedure).[43] The resulting charges are collected in sample PDB file deposited as supplementary material.

System 1 (the quantum region) consisted of side chains of His26, Tyr34, His81, Gln146, Asp167, His171, the Mn ion, the water/hydroxide ligand, and another water molecule (*cf.* Figs. 1, 2, and 4).

2.3. Quantum chemical calculations. All density functional theory (DFT) calculations reported in this study were carried out using the Turbomole 5.7 program.[44] The Perdew–Burke–Ernzerhof functional (PBE)[45] and Becke's three-parameter hybrid functional (B3LYP)[46] were used throughout. The PBE calculations were expedited by expanding the Coulomb integrals in an auxiliary basis set (the resolution-of-identity approximation, RI-J).[47,48] This method is denoted RI-PBE. All the geometry optimizations were carried out at the RI-PBE level using the 6-31G(d) basis set for all atoms,[49] except for manganese, for which we used the DZP basis sets of Schäfer *et al*[50] (referred to as the DZP basis set). The structures were optimized until the change in energy between two iterations was below 2.6 $J.mol^{-1}$ (10^{-6} a.u.) and the maximum norm of the internal gradients was below 5.0 $kJ.mol^{-1}Å^{-1}$ (10^{-3} a.u). More accurate energies were then estimated by single-point calculations **at the B3LYP level** using a larger basis set:

TZVP (triple-zeta valence with one polarization function on each atom)[51] except for manganese, for which 6-311+G(2d,2p) basis set[52] was used (referred to as the TZP basis set). Zero-point energies, thermal corrections to the Gibbs free energy, and entropic terms were obtained from a normal mode analysis on small *in vacuo* models (including manganese, one acetate, three imidazoles, and the metal-bound solvent molecule) of active site using the same method and software as for the geometry optimizations at the RI-PBE/DZP level, 298.15 K, and 1 atm pressure, and an ideal-gas rigid-rotor/harmonic-oscillator approximation.[53]

The spin-flip broken-symmetry DFT approach[54] was applied for the low-spin transition metal complexes, for which the standard unrestricted DFT calculations tend to converge to ionic rather than radical electron configurations. For this purpose the B3LYP functional and TZP basis set were used within ORCA program package.[55]

The complete active space self-consistent field (CASSCF),[56] and complete active space second-order perturbation theory (CASPT2)[57] calculations were carried out using the MOLCAS 7.0 program.[58] The protein was represented by an array of point charges (systems 2 and 3 in QM/MM). For all atoms, ANO-S basis set (contracted to [6s4p3d2f] for Mn; [3s2p] for O, N, and C; and [2s] for H) was used.[59] In CASSCF calculations, we used an active space of seven molecular orbitals (corresponding to the five Mn 3*d* orbitals and two O_2 π^* orbitals), occupied by seven or eight active electrons (depending on the Mn redox state). To expedite these calculations, the Cholesky decomposition of two-electron integrals with the default parameters in the MOLCAS 7.0 program was used.[60] For the S = 3/2, 5/2 and 7/2 spin states, state-specific CASSCF/CASPT2 calculations were carried out, whereas for the S = 2 spins states, state-averaged CASSCF and multi-state MS-CASPT2 calculations were performed (two states corresponding to $Mn^{II}\cdots HO_2^{\bullet}$ and $Mn^{III}\cdots HO_2^{-}$ electronic configurations) were taken into consideration because a two-state reaction pathway is involved).

In all CASSCF calculations, a level shift of 0.1 a.u. was used to improve the convergence of the multireference wave function. In the CASPT2 calculations, an imaginary level shift of 0.1 a.u. was used to eliminate intruder states.[61]

2.4. Molecular dynamics calculations. MD calculations were carried out using AMBER8 program. B onds involving hydrogen atoms were kept fixed at their equilibrium value by the SHAKE algorithm. The time step in the MD simulations was 1.5 fs. The temperature was kept constant at 300 K using a weak coupling to a temperature bath with a time constant of 1 ps.[62] A cut-off for the non-bonded interactions of 15 Å was employed. The 1-4 electrostatic and van der Waals interactions were scaled by a factor of 1.2 and 2.0, respectively. A dielectric constant of 1.0 was used in all simulations.

3. Results

3.1. Electronic structures of the $[MnX_n]^{2+/3+}$ and $[MnX_n\cdots O_2^{\bullet -}]^{2+/3+}$ complexes. The Mn(II) and Mn(III) ions contain five and four unpaired *d* electrons in their valence shell, respectively, which may give rise to three spin states (S = 1/2, 3/2, 5/2 for Mn(II), and S = 0, 1, 2 for Mn(III) complexes). Besides, they can couple with one or two unpaired electrons from the $O_2^{\bullet -}$ or $^3O_2$ moieties. The unambiguous assignment of the spin patterns in both the native and intermediate states of SODs is a challenging task both for experimental and computational chemists.[17] However, such a comprehensive study is not the primary aim of this work and we have selected the relevant spin states based on our previous work on small models of active site[35] and experimental evidence.[17] The investigated spin states are depicted in Schemes 1 and 2.

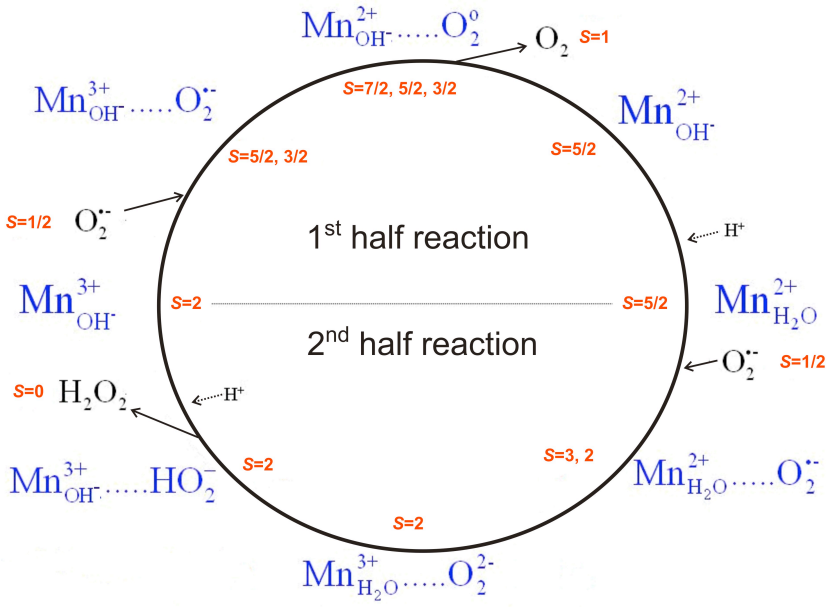

Scheme 1. The two disproportionation reactions involved in the catalytic cycle of MnSOD: oxidation of the $O_2^{\bullet-}$ substrate (first half reaction) and its reduction (second half reaction). For each structure, plausible protonation and spin states are indicated.

In spite of the multireference character of many of the studied electronic states, we expect the DFT method to give an adequate description of the QM part. Notably, B3LYP functional is generally recognized as one of the most accurate functionals for energies[63] and it has been shown to yield the correct spin multiplicity of the ground states in the few cases where a direct comparison with experimental data for MnSOD was possible.[35] This assumption is also justified *a posteriori*, by a comparison of the B3LYP and CASPT2 results. Therefore, only QM(B3LYP/TZVP)/MM energies are discussed in the following (if not stated otherwise). For the assignment of formal oxidation states for the individual manganese centers and O_2-derived ligands, electron spin densities, ρ_S, have been examined. For manganese, these are known to correlate with formal oxidation states of the metal centre (*i.e.*, Mn(II) and Mn(III) states are characterized by $\rho_S \approx 5$ and 4, respectively).[35,64] The studied spin states and corresponding electronic configurations are summarized in Scheme 2.

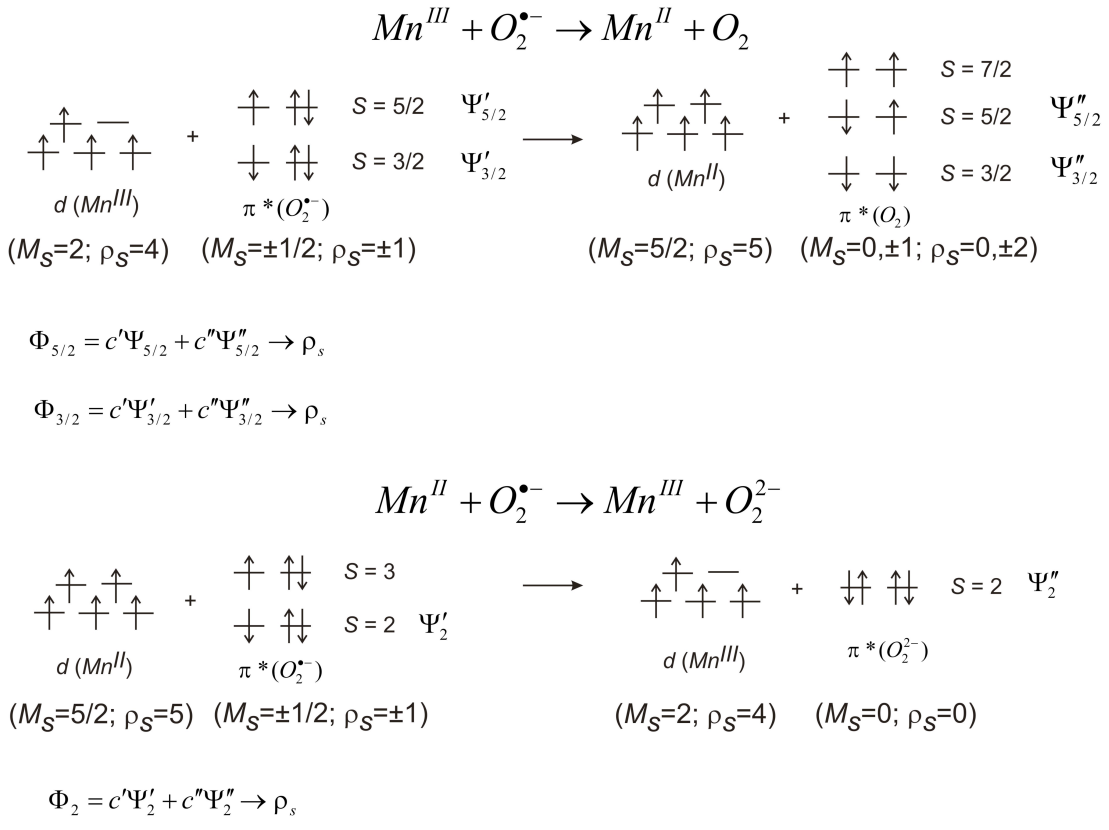

Scheme 2. The most relevant electronic configurations and corresponding spins of the species involved in the two half-reactions of MnSOD. In case of low-spin states, a strong mixing of different configurations often occurs along reaction pathway, schematically depicted here as a mixing of two configurations. The schematically depicted splitting of *d* orbitals of Mn ions is arbitrarily chosen to correspond to the O_h symmetry.

In the next parts, the results for three studied reaction mechanisms are presented, whereas the discussion related to the full reaction cycle of MnSOD can be found in the Discussion section.

3.2. Dissociative mechanism. We will start by examining the dissociative mechanism (denoted DIS). In this mechanism, the O_2 ligand replaces the Mn-bound solvent molecule (Figure 2). The calculated relative energies, as well as spin densities on manganese and on the O_2, HO_2, or H_2O_2 moieties for the

most stable equilibrium structures are compiled in Table 1. Each structure is denoted by a capital letter, corresponding to the notation introduced in Figure 2.

Table 1. Spin densities ρ_S on the O_2 ligand and central Mn atom and relative energies (total QM/MM energy, as well as the contributions from the protein relaxation, i.e., the molecular mechanics term - $\Delta E_{MM23} = E_{MM123} - E_{MM1}$, and the energy of the QM system *in vacuo* - $\Delta E_{vac\text{-}QM}$), calculated by the QM/MM method for structures involved in *dissociative* (DIS) mechanism. The capital letters correspond to the structures depicted in Figure 2. All data were obtained using B3LYP/TZP method for the QM part.

	Structure	S	ρ_s(Mn)	ρ_s(O_2)	ΔE_{MM23} [kJ·mol^{-1}]	$\Delta E_{vac\text{-}QM}$ [kJ·mol^{-1}]	$\Delta E_{QM/MM}$ [kJ·mol^{-1}]
$\mathbf{A_{dis}}$	$[Mn^{III}\cdots O_2^{\bullet-}]$	**3/2**	4.25	-1.17	0.0	0.0	0.0
	$[Mn^{III}\cdots O_2^{\bullet-}]$	**5/2**	4.24	0.80	0.0	26.2	25.9
$\mathbf{B_{dis}}$	$[Mn^{II}\cdots {}^3O_2]$	**3/2**	4.96	-1.89	8.7	21.2	33.9
	$[Mn^{II}\cdots {}^1O_2]$	**5/2**	4.92	0.06	8.7	61.3	74.9
	$[Mn^{II}\cdots {}^3O_2]$	**7/2**	5.00	1.91	8.7	24.9	38.5
$\mathbf{C_{dis}}$	$[Mn^{II}\cdots O_2^{\bullet-}]$	**2**	4.92	-0.93	0.0	31.9	9.6
	$[Mn^{II}\cdots O_2^{\bullet-}]$	**3**	4.91	1.04	0.0	27.5	5.4
$\mathbf{D_{dis}}$	$[Mn^{III}\cdots O_2^{2-}]$	**2**	4.05	0.06	-4.5	0.0	0.0
	$[Mn^{II}\cdots O_2^{\bullet-}]$	**3**	4.88	1.04	-4.5	143.5	147.2
$\mathbf{E_{dis}}$	$[Mn^{III}\cdots HO_2^{-}]$	**2**	4.14	-0.14	0.0	0.0	0.0
	$[Mn^{II}\cdots HO_2^{\bullet}]$	**3**	4.87	0.90	0.0	225.5	243.0
$\mathbf{E'_{dis}}$[a]	$[Mn^{II}\cdots HO_2^{\bullet}]$	**2**	4.92	-0.92	12.2	38.0	65.6
	$[Mn^{II}\cdots HO_2^{\bullet}]$	**3**	4.94	1.00	12.2	44.7	74.1
$\mathbf{G_{dis}}$	$[Mn^{III}\cdots H_2O_2]$	**2**	4.09	-0.10	0.0	0.0	0.0
	$[Mn^{II}\cdots H_2O_2^{\bullet+}]$	**3**	4.90	0.02[b]	0.0	99.6	132.6

[a] Structure $\mathbf{E'_{dis}}$ is similar to $\mathbf{E_{dis}}$, but with a Mn-OOH distance of 2.31 Å. In $\mathbf{E_{dis}}$, the corresponding

distance is 1.83 Å. (*cf.* Supporting Information).

[b] A spin density of $\rho_S \approx 1$ is delocalized on the ligands.

Structures $\mathbf{A_{dis}}$ and $\mathbf{B_{dis}}$ correspond to the $Mn^{III}SOD\text{-}O_2^{\bullet-}$ and $Mn^{II}SOD\text{-}O_2$ forms in the first half-reaction, respectively. The spin state S = 3/2 is the most stable for structure $\mathbf{A_{dis}}$. The spin densities indicate that it consists of a superoxide radical antiferromagnetically coupled to a high-spin (HS) Mn^{III} metal centre. The sextet spin state (S = 5/2) of $\mathbf{A_{dis}}$ is 26 kJ.mol^{-1} higher in energy and corresponds to the ferromagnetically coupled state. Similarly, the structure $\mathbf{B_{dis}}$ has the quartet (S = 3/2) ground state, which can be described as a dioxygen molecule $^3O_2$ antiferromagnetically coupled to a HS Mn^{II} ion. Comparing total QM/MM energies of these two consecutive reaction steps, we may conclude that the oxidation of $O_2^{\bullet-}$ to O_2 is endothermic by 34 kJ.mol^{-1}.

On the other hand, the reduction of $O_2^{\bullet-}$ to O_2^{2-} (structures $\mathbf{C_{dis}}$ and $\mathbf{D_{dis}}$) is exothermic by ~5 kJ.mol^{-1}. It can be accompanied by a change of the spin state from septet (S = 3) to quintet (S = 2), but these two states are almost degenerate for the $\mathbf{C_{dis}}$ structure.

Following the reaction cycle, the O_2^{2-} moiety should be protonated. In contrast to the other discussed reaction mechanisms, it is not clear where the first proton comes from in the dissociative mechanism. However, an energy comparison of structures $\mathbf{E_{dis}}$ and $\mathbf{E'_{dis}}$ corresponding to $Mn^{III}SOD\text{-}O_2H^-$ and $Mn^{II}SOD\text{-}O_2H^{\bullet}$, respectively, allows us to decide whether the electron transfer precedes the protonation or vice-versa. It can be seen that $\mathbf{E_{dis}}$ is ~70 kJ.mol^{-1} more stable than $\mathbf{E'_{dis}}$ (see Table 1). This difference rules out the possibility that the superoxide is first protonated and then undergoes the reduction. This difference is similar to the corresponding value of 59 kJ.mol^{-1} for the small first-sphere models reported in the previous work.[35]

The structure $\mathbf{G_{dis}}$ corresponds to the terminal step of the whole catalytic cycle, following the addition of the second proton. The calculated Mn-O equilibrium distances suggest that H_2O_2 binds weaker to $\mathbf{G_{dis}}$ than HO_2^- to $\mathbf{E_{dis}}$ (R(Mn-O) = 2.06 Å in $\mathbf{G_{dis}}$ *vs.* 1.83 Å in $\mathbf{E_{dis}}$).

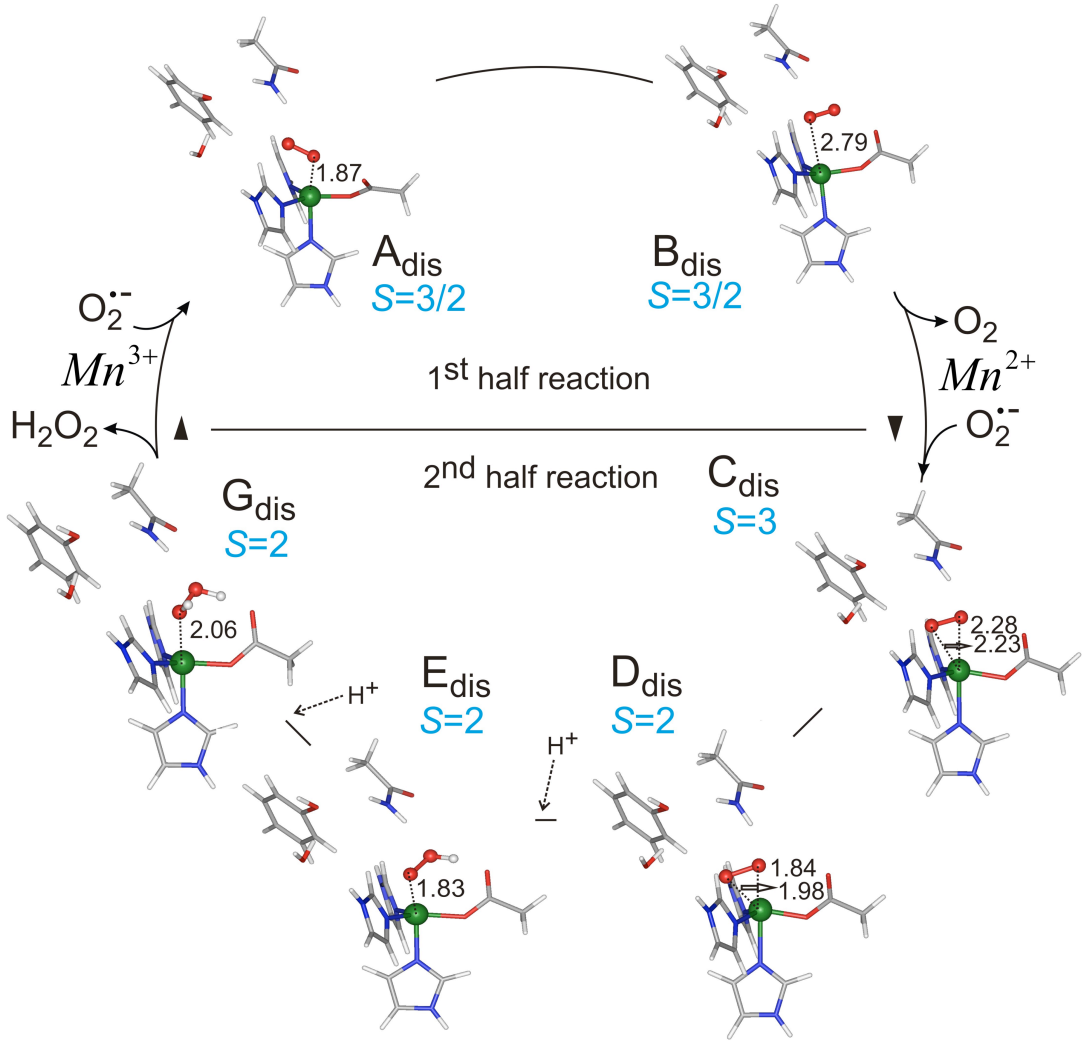

Figure 2. Dissociative reaction mechanism as obtained by the QM/MM calculations. The key structures in the catalytic cycle are depicted together with the total spin quantum numbers of the corresponding ground states. The metal–oxygen distances are in Å.

3.3. Associative mechanism. Next, we studied the associative (AS) mechanism, characterized by the O_2 binding as the sixth ligand to Mn centre. The calculated data for the intermediates involved in the associative mechanism are compiled in Table 2 and the corresponding structures are depicted in Figure 3.

Table 2. Spin densities ρ_S on the O_2 ligand and central Mn atom, and relative energies (total QM/MM energy, as well as the contributions from the protein relaxation, i.e., molecular mechanics

term - $\Delta E_{MM23} = E_{MM123} - E_{MM1}$, and the energy of the QM system *in vacuo* - $\Delta E_{vac\text{-}QM}$), calculated by QM/MM method for structures involved in *associative* (AS) mechanism. The capital letters correspond to the structures depicted in Figure 3. All data were obtained using B3LYP/TZP method for the QM part.

	Structure	*S*	ρ_S(Mn)	ρ_S(O_2)	ΔE_{MM23} [kJ·mol^{-1}]	$\Delta E_{vac\text{-}QM}$ [kJ·mol^{-1}]	$\Delta E_{QM/MM}$ [kJ·mol^{-1}]
$\mathbf{A_{as}}$	$[Mn^{III}{}_{OH\text{-}}\cdots O_2^{\bullet-}]$	**3/2**	4.00	-1.07	0.0	0.0	0.0
	$[Mn^{III}{}_{OH\text{-}}\cdots O_2^{\bullet-}]$	**5/2**	4.06	0.90	0.0	2.7	12.0
$\mathbf{B_{as}}$	$[Mn^{II}{}_{OH\text{-}}\cdots {}^3O_2]$	**3/2**	4.61	-1.60	-9.9	2.8	6.1
	$[Mn^{II}{}_{OH\text{-}}\cdots {}^1O_2]$	**5/2**	4.81	0.14	-9.9	44.4	30.2
	$[Mn^{II}{}_{OH\text{-}}\cdots {}^3O_2]$	**7/2**	4.93	1.98	-9.9	3.7	-3.1
$\mathbf{C_{as}}$	$[Mn^{II}{}_{H2O}\cdots O_2^{\bullet-}]$	**2**	4.83	-0.90	0.0	coming soon	0.9
	$[Mn^{II}{}_{H2O}\cdots O_2^{\bullet-}]$	**3**	4.92	1.02	0.0	0.0	0.0
$\mathbf{D_{as}}$	$[Mn^{III}{}_{H2O}\cdots O_2^{2-}]$	**2**	4.26	-0.28	-3.8	7.1	-0.5
	$[Mn^{II}{}_{H2O}\cdots O_2^{\bullet-}]$	**3**	4.85	1.05	-3.8	113.7	112.9
$\mathbf{E_{as}}$	$[Mn^{III}{}_{H2O}\cdots HO_2^{-}\cdots TyrO^{-}]$	**2**	4.13	-0.17	-5.2	97.2	90.0
	$[Mn^{II}{}_{H2O}\cdots HO_2^{\bullet}\cdots TyrO^{-}]$	**3**	4.81	0.88	-5.2	260.1	252.4
$\mathbf{F_{as}}$	$[Mn^{III}{}_{OH\text{-}}\cdots HO_2^{-}]$	**2**	4.00	-0.03	-3.7	-18.2	-17.3
	$[Mn^{II}{}_{OH\text{-}}\cdots HO_2^{\bullet}]$	**3**	4.01	0.04	-3.7	263.1	255.5
$\mathbf{E^*_{as}}$	$[Mn^{III}{}_{OH\text{-}}\cdots H\cdots HO_2^{-}]$	**2**	4.03	-0.07	-3.4	24.9	21.2
	$[Mn^{II}{}_{OH\text{-}}\cdots H\cdots HO_2^{\bullet}]$	**3**	4.81	1.00	-3.4	182.5	163.5
$\mathbf{F^*_{as}}$	$[Mn^{III}{}_{OH\text{-}}\cdots HO_2^{-}]$	**2**	3.94	0.00	-0.4	-21.7	-15.0
	$[Mn^{II}{}_{OH\text{-}}\cdots HO_2^{\bullet}]$	**3**	4.70	1.01	-0.4	264.2	255.7
$\mathbf{G_{as}}$	$[Mn^{III}{}_{OH\text{-}}\cdots H_2O_2]$	**2**	4.00	0.01	0.0	0.0	0.0
	$[Mn^{II}{}_{OH\text{-}}\cdots H_2O_2^{\bullet+}]$	**3**	4.83	0.14[a]	0.0	309.4	316.3

[a] Spin density of $\rho_S \approx 1$ is delocalized onto the ligands.

Comparing the QM/MM energies of structures $\mathbf{A_{as}}$ and $\mathbf{B_{as}}$, it can be seen that the oxidation of $O_2^{\bullet-}$ to O_2 is exothermic by 3 kJ.mol^{-1}. The $\mathbf{A_{as}}$ state has a quartet ground state as in the DIS mechanism. However, for the $\mathbf{B_{as}}$ structure, the octet state is 9 kJ.mol^{-1} lower in energy than the quartet state. It can be characterized as a $^3O_2$ molecule ferromagnetically coupled to a HS Mn^{II} ion. In Figure 4, the QM/MM energy profiles along a pathway defined by the Mn–O distance are depicted. For the octet state, the energy on the dissociation curve is monotonically decreasing, showing that $^3O_2$ does not bind to the Mn site. At a Mn–O distance of ~3 Å, it crosses the quartet state, and then becomes the ground state for the product $\mathbf{B_{as}}$ (*cf.* Table 2). The quartet–octet crossing is the highest point on QM/MM energy profile with an activation barrier of $\Delta E^{\neq} \approx 10$ kJ.mol^{-1} with respect to the ground state of reactant $\mathbf{A_{as}}$, which is certainly well below the experimental activation barrier of ~50 kJ/mol (as can be inferred from the k_{cat} values of 10^4-10^5 s^{-1} **xxx Add a reference**). The sextet is not the ground state at any Mn–O distance. Moreover, the spin densities at the Mn centre and O_2 molecule (Figure 4) indicate that the sextet state dissociates as a singlet dioxygen ($^1O_2$). This species is appreciably **xxx experimentally it is ~90 kJ/mol** less stable than $^3O_2$, which is the predicted dissociation product for the quartet and octet states of $\mathbf{B_{as}}$ complex.

The B3LYP calculations of the two-state reaction profile are in reasonable agreement with the CASPT2/CASSCF (7 electrons in 7 orbitals) results. QM(CASPT2)/MM predicts that the $\mathbf{A_{as}}$ sextet state lies 28 kJ.mol^{-1} above the quartet ground state. Likewise, $\mathbf{B_{as}}$ quartet and sextet states lie 1 and 5 kJ.mol^{-1} above octet ground state and the reaction barrier is estimated to be $\Delta E^{\neq} = 24$ kJ.mol^{-1} (the Mn–O distance in B3LYP transition-state structure is approximately 3 Å, whereas for CASPT2 it is closer to 2.6 Å). Formally, the quartet–octet crossing is spin-forbidden process, but it can be facilitated via the spin–orbit coupling (SOC) with a sextet state.

In the second half-reaction we investigated two mechanisms: A Tyr34/Gln146 mediated proton-transfer and a direct ($H_2O_{Mn\text{-}bound} \rightarrow O_2^{\bullet-}$) proton-transfer (denoted $AS_{RED}1$, $AS_{RED}2$; cf. Figure 3). Concerning the $AS_{RED}1$ mechanism, we optimized three putative intermediates, $\mathbf{C_{as}}$, $\mathbf{D_{as}}$, and $\mathbf{F_{as}}$, which

represent the initial $Mn^{II}_{H2O}O_2^{\bullet-}$ state, the $Mn^{III}_{H2O}O_2^{2-}$ state after internal electron transfer between Mn and $O_2^{\bullet-}$, and the Mn^{II}_{OH}-HO_2^- state after internal proton transfer from H_2O to O_2^{2-}, respectively. From Table 2, it can be seen that the QM/MM energies decrease by 17 kJ.mol^{-1} along this reaction path, and that the ground state is the septet, possibly except for $\mathbf{C_{as}}$, for which the quintet and septet states are degenerate. This suggests that this part of the second half-reaction, is exothermic in the $AS_{RED}1$ mechanism. As can be seen in Figure 3, a putative proton-transfer path involves Gln146, Tyr34, and the metal-bound water molecule. Therefore we also optimized the structure $\mathbf{E_{as}}$, as one of the likely intermediates along the stepwise pathway, with both the Mn-bound water and HO_2^- protonated, but Tyr34 deprotonated and Gln146 protonated. However, such a state is ~90 kJ.mol^{-1} higher in energy than structure $\mathbf{C_{as}}$, which makes this pathway less likely. Of course, there are many alternative (partly) concerted or step-wise mechanism involving the transfer of the four protons, which opens an enormous number of possibilities to be studied. A careful investigation of such mechanism is beyond the scope of this study. However, we strongly believe that this mechanism can be ruled out based on the high energy of the $\mathbf{E_{as}}$ state. A transition-state structure on the concerted pathway must involve structure that would involve deplanarization of Gln146 (formation of a $-CONH_3^+$), which is energetically favorable. We would expect this pathway to be competitive mechanism only if tunneling effects are significant. However, kinetic isotope effect (KIE) measurements of the whole reaction (up to release of H_2O_2) do not provide any direct evidence of tunneling – the solvent k_H/k_D ratio is approximately 2.[65]

Therefore, we next tested the other associative mechanism for the second half reaction, denoted $AS_{RED}2$. It involves an electron transfer ($\mathbf{C_{as}} \rightarrow \mathbf{D_{as}}$) followed by a direct proton transfer from metal-bound water molecule to metal-bound peroxide anion, resulting in structure $\mathbf{F^*_{as}}$. This mechanism has previously been studied and discussed for a small gas-phase model of the MnSOD and FeSOD active site.[66] The PES scan of the $D \rightarrow E^*_{as} \rightarrow F^*_{as}$ process suggests the existence of a single activation barrier of 21 kJ.mol^{-1}. The reaction is exothermic (ΔE = -15 kJ.mol^{-1}). **Xxx This is very unclear. As far as I can see, 21 kJ is the energy of E*as (the activation energy is expected to be higher) and -15 kJ/mol is the energy of F*as (as it should be). I suggest that you include a figure of the PES, showing the**

actual activation energy. Thus, the activation barrier strongly favors this reaction mechanism before the $AS_{RED}1$ mechanism.'. Finally, it can be noticed that the high energy of the septet spin states compared to the quintet ground states of structure **G_{as}** excludes the possibility of protonation of $O_2^{\bullet-}$ prior to its reduction. **MS: CASPT2 results coming soon... hopefully! I am aware that no Figure with the scan of the PES is shown, but I think that mechanism is evident from Figure 3 and numbers are given in the text.**

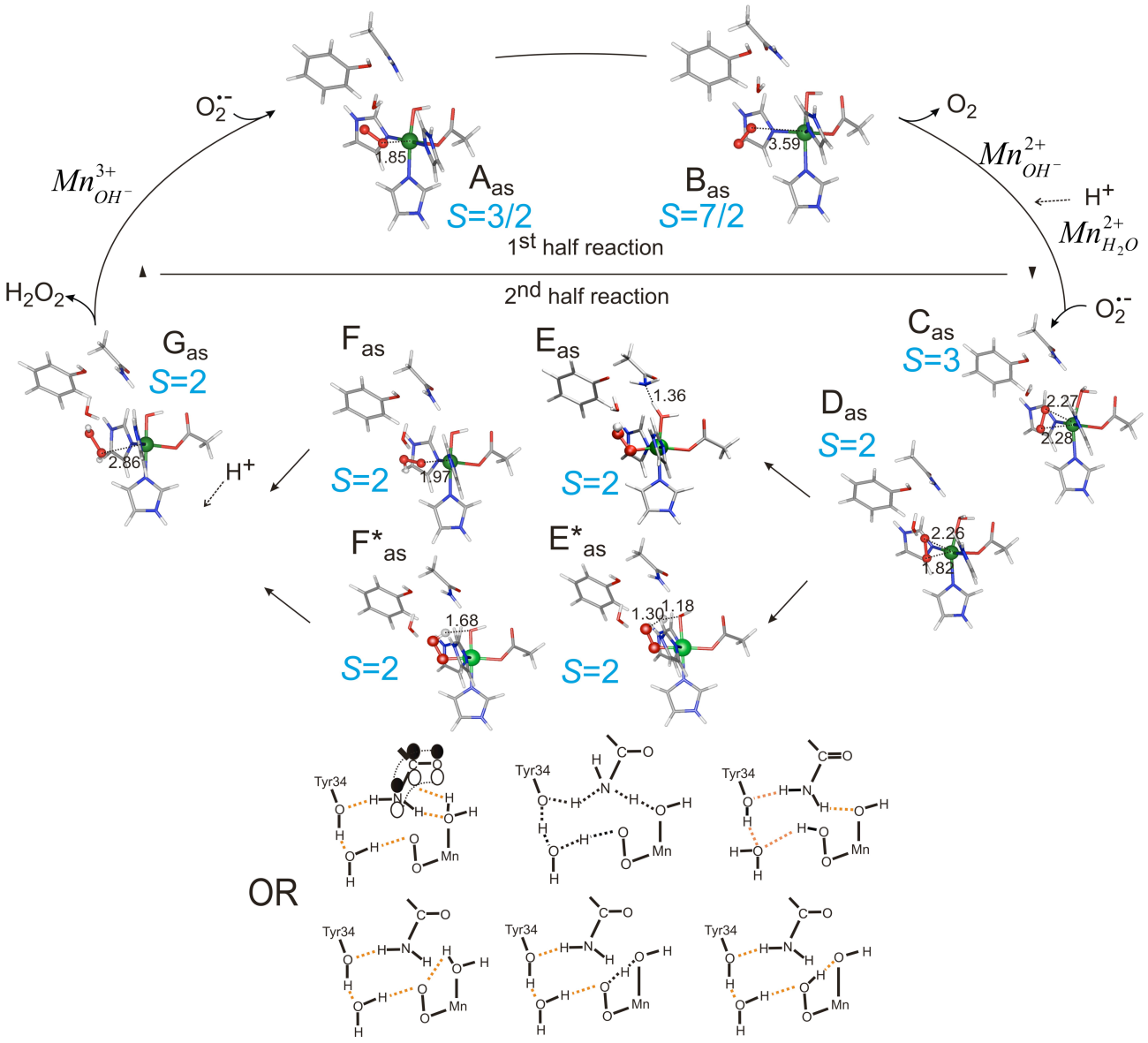

Figure 3. Key structures involved in the *associative reaction pathway* (AS) obtained by the QM/MM calculations (the total spin quantum numbers of the corresponding ground states are depicted). The Mn–O distances are in Å. The putative proton-transfer pathway from the metal-bound water molecule to the superoxide radical-anion is depicted in the lower part of the scheme.

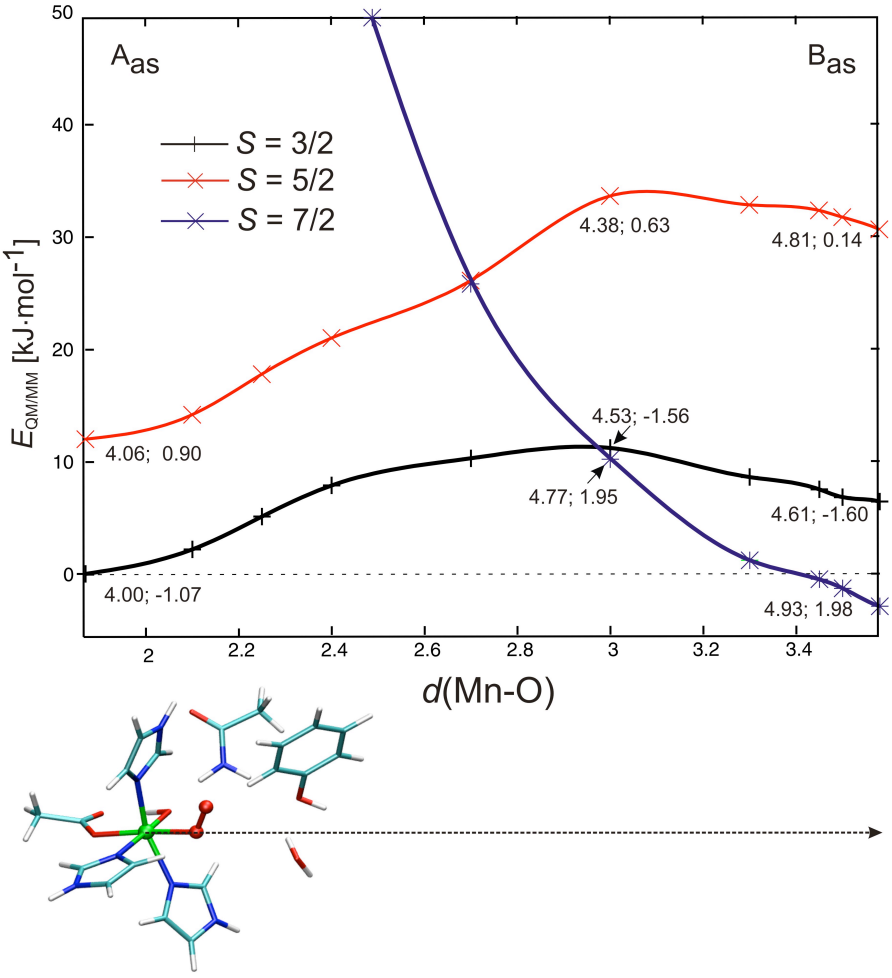

Figure 4. The QM/MM potential energy profiles corresponding to the release of O_2 moiety from the active site for an associative complex. The numbers in the graph denote the spin densities at the manganese and O_2 centers. Their contributions to the relevant electronic configurations are shown in Scheme 2.

3.4 Second-sphere mechanisms Finally, we studied two different second-sphere mechanisms. The

second sphere mechanism has been proposed on the basis of several experimental observations concerning the binding of nonnative substrates (such as NO, N_3^- and F^-) in the active site.[24,25,26,27] To identify plausible $O_2^{\bullet-}$ second-sphere interaction sites, we run 45 ps molecular dynamics simulation (with the manganese ion and the five atoms directly coordinated to it kept fixed**)**, followed by QM/MM optimization (snapshots of the enzyme structure taken every 5 ps). In the first pathway, denoted SS1, $O_2^{\bullet-}$ is hydrogen-bonded to the OH group of the Tyr-34 residue, whereas in the second pathway (SS2), $O_2^{\bullet-}$ is hydrogen-bonded to the metal-bound water molecule or hydroxide anion (*cf.*, Figures 5 and 6).

For the first half reaction, the pathway from $\mathbf{A_{SS1}}$ to $\mathbf{B_{SS1}}$ is characterized by an increase in the QM/MM energy of 42 kJ.mol^{-1}, which makes it less favorable, compared to the AS mechanism. Contrary to the AS, the $S = 3/2$ state remains the ground state of the system even after the transfer of one electron from Mn centre to O_2 species. The inexpedience of the $\mathbf{A_{SS1}} \rightarrow \mathbf{B_{SS1}}$ reaction step is supported by the fact that the electronic coupling, H_{AB}, as well as the rate of electron transfer ($k_{ET} \sim H_{AB}^2$) decrease exponentially with increasing donor–acceptor separation,[67] This should disfavor the SS1 mechanism (with a Mn–O distance of ~8 Å) with respect to alternative AS or DIS mechanisms for the first half-reaction.

For the SS2 mechanism, the $\mathbf{A_{SS2}} \rightarrow \mathbf{B_{SS2}}$ redox process is energetically favorable ($\Delta E_{QM/MM}$ = -16 kJ.mol^{-1}), with the triplet state being the most stable for both structures. However, the energy of $\mathbf{A_{as}}$ is about 30 kJ.mol^{-1} lower than the energy of $\mathbf{A_{SS2}}$ intermediate, indicating that first-sphere binding of $O_2^{\bullet-}$ is more favorable than second-sphere binding. The main contribution to this energy difference comes from the preference of the metal-bound hydroxide anion to form a hydrogen bond to the carboxyl group of the Asp167 ligand, rather than to $O_2^{\bullet-}$. Therefore, this comparison disfavors the second-sphere mechanism for the first half-reaction.

Table 3. Spin densities ρ_S on the O_2 ligand and the central Mn atom, and relative energies (total QM/MM energy, as well as the contributions from the protein relaxation, i.e., molecular mechanics term - $\Delta E_{MM23} = E_{MM123} - E_{MM1}$, and the energy of the QM system *in vacuo* - $\Delta E_{vac\text{-}QM}$), calculated

by the QM/MM method for structures involved in the two *second-sphere* (SS1, SS2) mechanisms. The capital letters correspond to the structures depicted in Figures 5 and 6. All data were obtained using B3LYP/TZP method for the QM part.

	SS1	***S***	ρ_S(Mn)	ρ_S(O_2)	ΔE_{MM23} [kJ·mol^{-1}]	$\Delta E_{vac\text{-}QM}$ [kcal·mol^{-1}]	$\Delta E_{QM/MM}$ [kJ·mol^{-1}]
$\mathbf{A_{SS1}}$	$[Mn^{III}_{OH\text{-}}\cdots O_2^{\bullet-}]$	**3/2**	4.02	-1.00	0.0	0.0	0.0
	$[Mn^{III}_{OH\text{-}}\cdots O_2^{\bullet-}]$	**5/2**	4.03	1.00	0.0	-0.2	-0.2
$\mathbf{B_{SS1}}$	$[Mn^{II}_{OH\text{-}}\cdots {}^3O_2]$	**3/2**	4.76	-1.70	-13.7	4.2	42.3
	$[Mn^{II}_{OH\text{-}}\cdots {}^1O_2]$	**5/2**	4.71	0.38	-13.7	33.5	66.2
	$[Mn^{II}_{OH\text{-}}\cdots {}^3O_2]$	**7/2**	4.92	1.97	-13.7	13.2	67.4
$\mathbf{C_{SS1}}$	$[Mn^{II}_{H2O}\cdots O_2^{\bullet-}]$	**2**	4.98	-1.00	0.0	0.0	0.0
	$[Mn^{II}_{H2O}\cdots O_2^{\bullet-}]$	**3**	4.98	1.00	0.0	0.0 **xxx Is this**	0.0
$\mathbf{E_{SS1}}$	$[Mn^{III}_{OH\text{-}}\cdots HO_2^{-}]$	**2**	4.03	0.08	0.6	173.6	141.2
	$[Mn^{II}_{OH\text{-}}\cdots HO_2^{\bullet}]$	**3**	4.89	0.73	0.6	221.8	236.1
$\mathbf{F_{SS1}}$	$[Mn^{III}_{OH\text{-}}\cdots HO_2^{-}]$	**2**	4.04	0.00	2.4	60.5	7.0
	$[Mn^{II}_{OH\text{-}}\cdots HO_2^{\bullet}]$	**3**	4.85	0.22[a]	2.4	216.1	226.2
$\mathbf{G_{SS1}}^*$	$[Mn^{III}_{OH\text{-}}\cdots H_2O_2]$	**2**	4.00	0.00	0.0	0.0	0.0
	SS2						
$\mathbf{A_{SS2}}$	$[Mn^{III}_{OH\text{-}}\cdots O_2^{\bullet-}]$	**3/2**	4.05	-1.05	0.0	0.0	0.0
	$[Mn^{III}_{OH\text{-}}\cdots O_2^{\bullet-}]$	**5/2**	4.01	1.00	0.0	4.5	1.2
$\mathbf{B_{SS2}}$	$[Mn^{II}_{OH\text{-}}\cdots {}^3O_2]$	**3/2**	4.86	-1.82	1.7	-43.8	-16.5
	$[Mn^{II}_{OH\text{-}}\cdots {}^1O_2]$	**5/2**	4.82	0.25	1.7	-7.7	19.4
	$[Mn^{II}_{OH\text{-}}\cdots {}^3O_2]$	**7/2**	4.92	1.90	1.7	-39.6	-11.9
$\mathbf{C_{SS2}}$	$[Mn^{II}_{H2O}\cdots O_2^{\bullet-}]$	**2**	4.85	-1.01	0.0	0.0	0.0
	$[Mn^{II}_{H2O}\cdots O_2^{\bullet-}]$	**3**	4.96	1.01	0.0	0.0	0.1
$\mathbf{F_{SS2}}$	$[Mn^{III}_{OH\text{-}}\cdots HO_2^{-}]$	**2**	3.93	0.00	10.5	77.6	47.8
	$[Mn^{II}_{OH\text{-}}\cdots HO_2^{\bullet}]$	**3**	4.84	0.60	10.5	250.1	291.1
$\mathbf{G_{SS2}}^*$	$[Mn^{III}_{OH\text{-}}\cdots H_2O_2]$	**2**	4.02	0.00	0.2	-0.1	-2.5

[a] A spin density of $\rho_s \approx 1$ is delocalized on the ligands.

* G_{SS2} is compared with G_{SS1}

The initial state in the second half reaction - the structure $\mathbf{C_{SS1}}$, characterized by $O_2^{\bullet-}$ bound to the hydroxyl group of the Tyr34 residue at a Mn–O distance of ~8 Å - is depicted in Figure 5. In this case, there is no preference for a specific spin state because of the large separation of the centers with unpaired electrons. The hydrogen-bond network around $\mathbf{C_{SS1}}$ is similar to that around $\mathbf{C_{as}}$, involving the Mn-bound water molecule, Gln146, Tyr34, and a water molecule, although in this case, $O_2^{\bullet-}$ is directly bound to Tyr34. Therefore, the mechanism of proton transfer from the metal-bound water molecule to the O_2 moiety might be similar to that in the associative mechanism (cf., Figure 5). The structure $\mathbf{E_{SS1}}$ is a putative intermediate in such a coupled electron- and proton transfer, where the amide group of the Gln-146 **xxx You are mixing Gln-146 and Gln146 (with and without a hyphen; also for other residues). Please, ensure that you are consistent.** residue is still distorted from its stable planar configuration. A stepwise proton transfer in the SS1 mechanism seems unfavorable, in analogy with the $AS_{RED}1$ mechanism. Although the final $Mn^{III}{}_{OH}\text{-}O_2H^-$ complex (structure $\mathbf{F_{SS1}}$) has similar QM/MM energy (ΔE = 7 kJ.mol^{-1}, see Table 3) as the initial $Mn^{II}{}_{H2O}\text{-}O_2^{\bullet-}$ complex (structure $\mathbf{C_{SS1}}$), the energy of $\mathbf{E_{SS1}}$ is 141 kJ.mol^{-1} higher than the initial complex (mainly due to the $sp^2 \rightarrow sp^3$ hybridization of $–NH_2$ group of Gln-146). This implies a prohibitively large energy barrier along this SS1 reaction pathway. It can be noticed that both the SS1 and $AS_{RED}1$ mechanisms suggest a participation of Tyr34 residue in proton-transfer network. It can be noted that it is not entirely clear from the experimental evidence, whether Tyr34 necessarily serves as the proton donor. For example, experiments with a fluorinated Tyr34 residue[68] indicate that Tyr34 does not play a role as proton donor (which would be in agreement with our arguments disfavoring $AS_{RED}1$ and SS1 mechanism). **Xxx And the Tyr34Phe mutant is 40% active.**

The SS2 pathway, on the other hand, offers much simpler mechanism of proton transfer (*cf.* Figure 6). It involves only a single step, $\mathbf{C_{SS2}} \rightarrow \mathbf{F_{SS2}}$, starting from the $Mn^{II}{}_{H2O}O_2^{\bullet-}$ structure in the degenerate

quintet or septet states, and ending up in the $Mn^{II}_{OH}HO_2^-$ structure in the quintet state. Mapping QM/MM potential-energy surface by a relaxed two-dimensional scan along the two reaction coordinates $HO^{\cdots}H^{\cdots}O_2$, we obtain a reaction energy profile that involves the crossing of two quintet states, depicted in Figure 7. It can be seen that the transition state (characterized by $HO^{\cdots}H_2 \approx 1.4$ Å and $H^{\cdots}O_2 \approx 1.1$ Å) lies 62 kJ.mol^{-1} above the $\mathbf{C_{SS2}}$ state. This value is in resonable agreement with the experimental activation barrier (~50 kJ.mol^{-1}). Moreover, following the pathway to the structure $\mathbf{F_{SS2}}$ on the two-dimensional surface, we observe a spontaneous proton transfer from the Tyr34-OH to HO_2^- species, resulting in the $Tyr34\text{-}O^{-\cdots}HOOH^{\cdots}OH_{(Mn\text{-}bound)}$ arrangement. The QM(CASSCF/CASPT2/ANO-S)/MM (8 electrons in 7 orbitals) benchmark calculations yielded a reaction energy of 35 kJ.mol^{-1} and an activation energy of 67 kJ.mol^{-1}, thus confirming the results obtained by using DFT(B3LYP) method. Although the barrier is 41 kJ.mol^{-1} higher than the barrier of the associative $AS_{RED}2$ mechanism, which is described by the direct proton transfer from metal-bound water molecule to metal-bound O_2^{2-}anion, the initial $\mathbf{C_{SS2}}$ structure lies 43 kJ.mol^{-1} below $\mathbf{C_{as}}$. Therefore, using our QM/MM model, we predict that both $AS_{RED}2$ and SS2 mechanisms are possible pathways in the second half-reaction of MnSOD catalytic cycle. It can be noted that qualitative entropy considerations might slightly favor the SS2. Finally, the two H_2O_2-protein structures, $\mathbf{G_{SS1}}$ and $\mathbf{G_{SS2}}$, are almost isoenergetic and are comparable to $\mathbf{G_{as}}$.

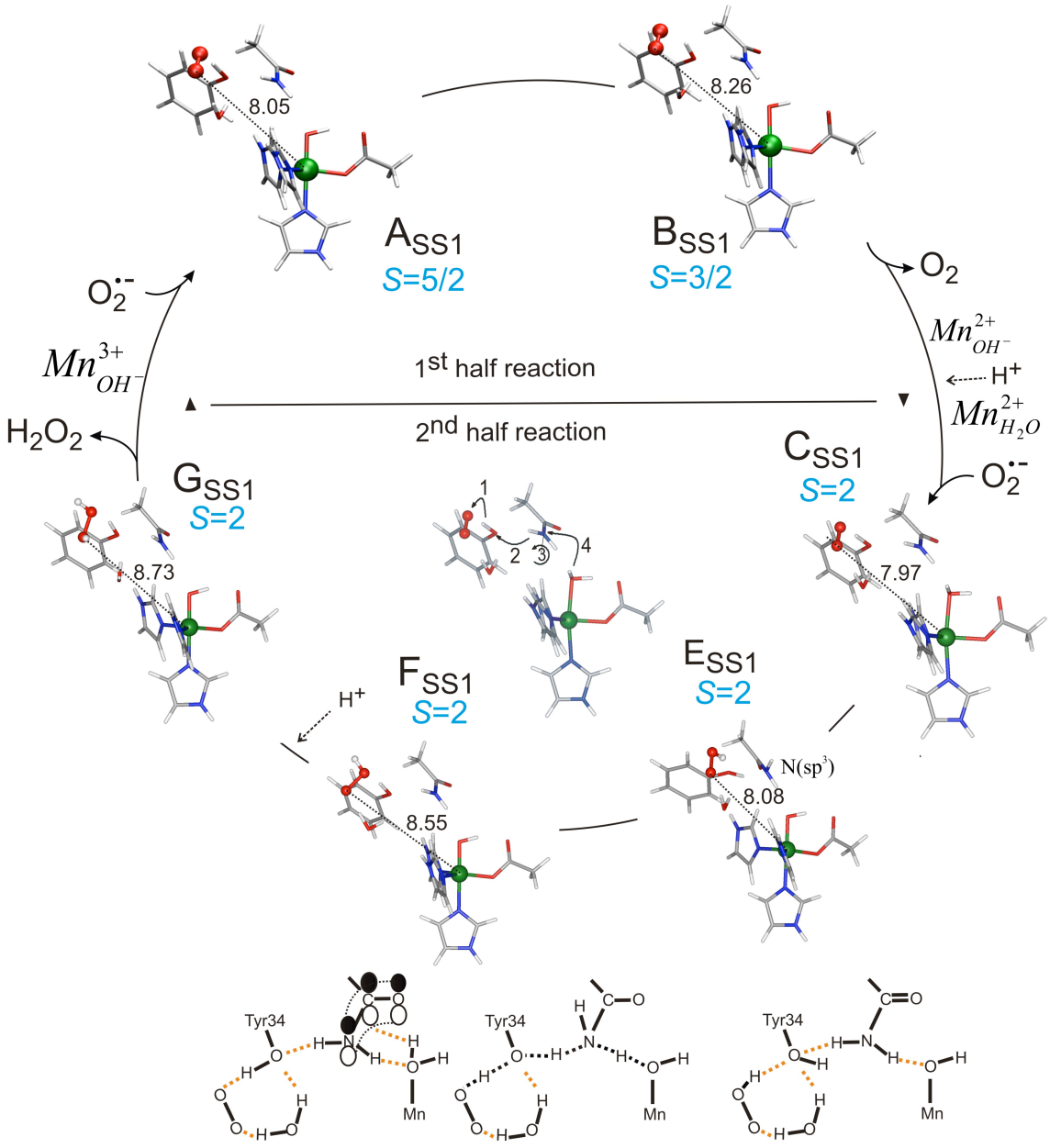

Figure 5. Key structures involved in the first *second-sphere* reaction pathway (SS1) as obtained by QM/MM calculations (the total spin quantum numbers of the corresponding ground states are depicted). The metal–oxygen distances are in Å. The putative proton-transfer pathway from the metal-bound water molecule to $O_2^{\bullet-}$ is depicted in the lower part of the scheme.

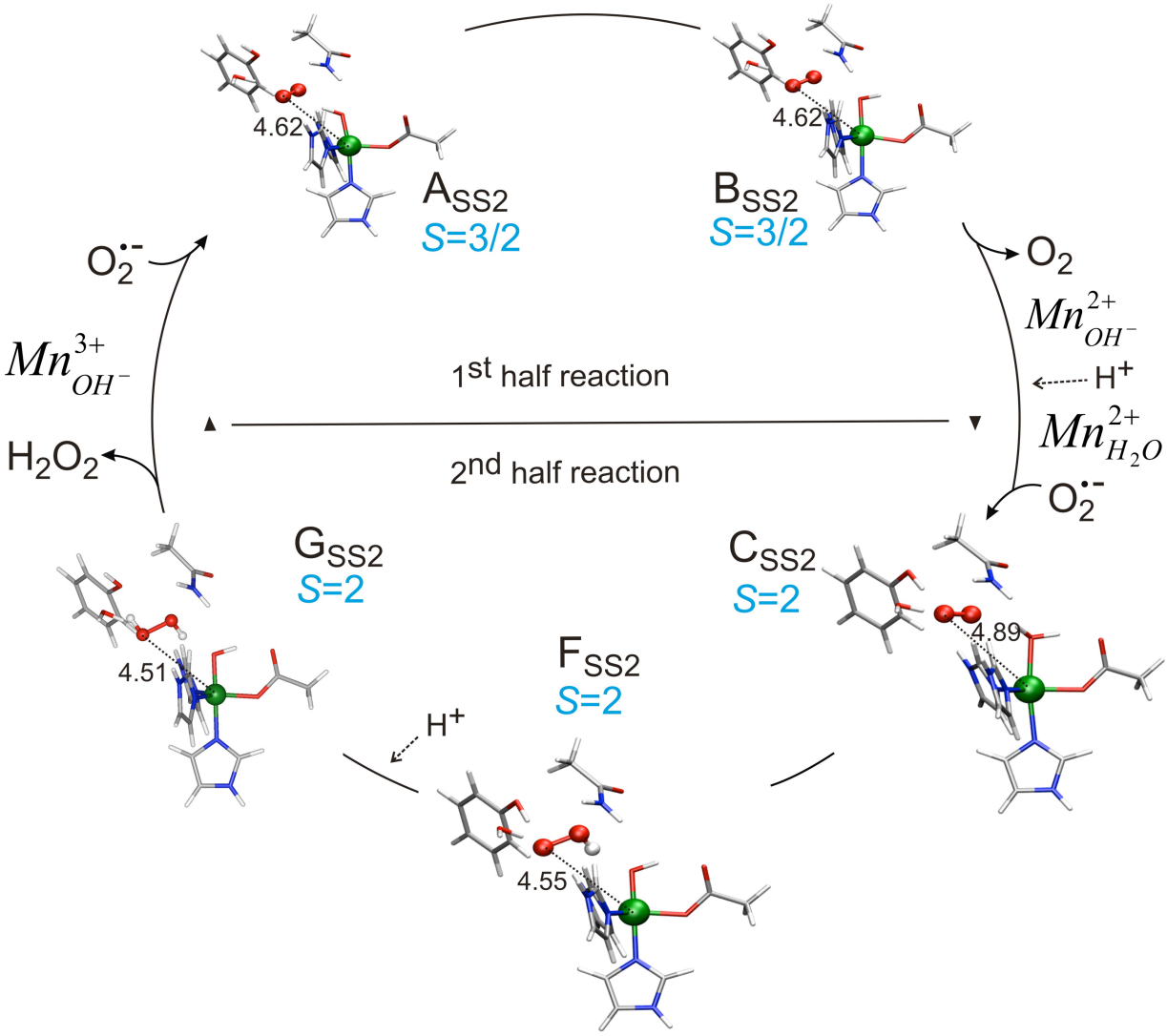

Figure 6. Key structures involved in the second *second-sphere* reaction pathway (SS2), as obtained by QM/MM calculations (the total spin quantum numbers of the corresponding ground states are depicted). The metal–oxygen distances are in Å.

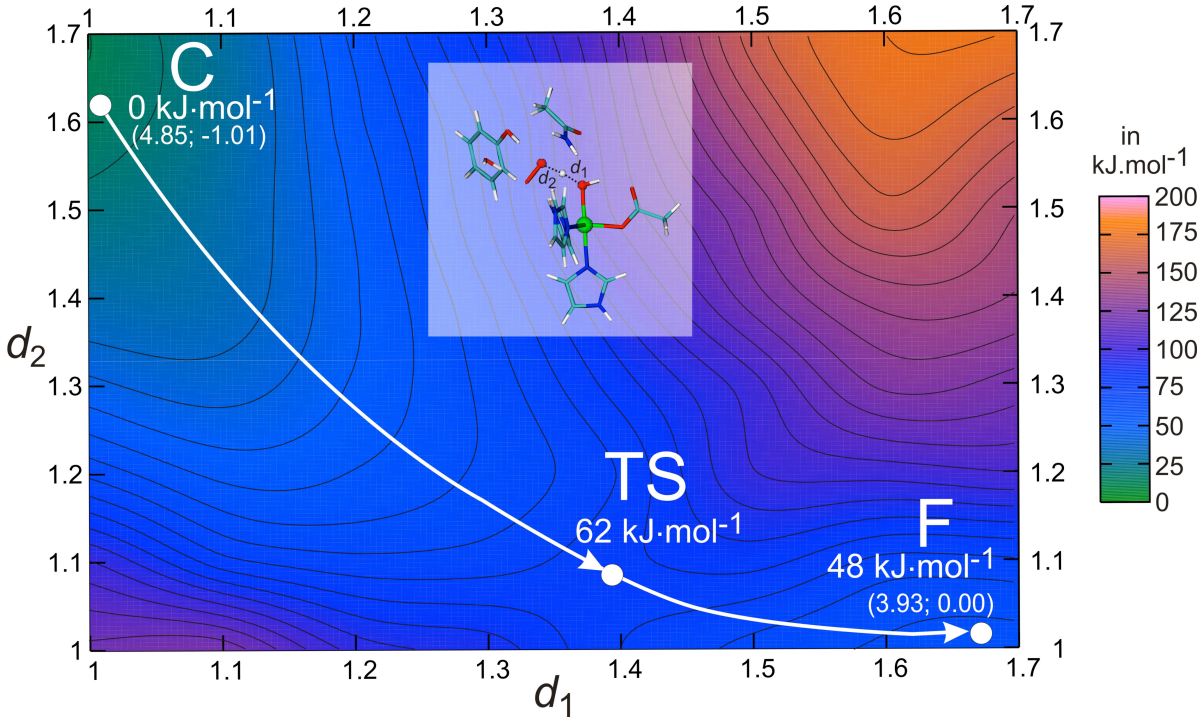

Figure 7. The two-dimensional QM(B3LYP/6-31G*)/MM potential-energy surface of the proton-coupled electron transfer from Mn–OH_2 to O_2 in the SS2 mechanism. The interatomic distances are in Å. The numbers (x; y) in the graph depict the spin densities at the manganese and O_2 centers. Their contributions to the relevant electronic configurations are shown in Scheme 2.

4. Discussion

4.1. First half-reaction: oxidation of $O_2^{\bullet-}$ to O_2. In the previous sections, we have described the three possible mechanisms for the SODs (dissociative, associative, and second-sphere). In this section, we will compare the three mechanisms in order to decide which is most plausible of them. To be able to compare their energies, the ground (triplet) spin state was chosen as the reference. It is straightforward to compare the energies of the $\mathbf{A_{as}}$, $\mathbf{A_{SS1}}$ and $\mathbf{A_{SS2}}$ structures, because they contain the same atoms, but it is more problematic to include $\mathbf{A_{dis}}$ in the comparison. The best that can be done in order to make $\mathbf{A_{dis}}$ comparable with three other structures is to sum the energy of one hydroxide anion solvated in water-like environment (ε_r = 80 within COSMO approach **xxx Add reference**) with QM/MM energy of $\mathbf{A_{dis}}$. Then, the complex stability decreases in the following order $\mathbf{A_{SS1}} < \mathbf{A_{as}} < \mathbf{A_{SS2}} < \mathbf{A_{dis}}$ (0, 24, 53 and 82

kJ.mol^{-1}; the energy of the $\mathbf{A_{dis}}$ state is probably stabilized by up to ~55 kJ.mol^{-1} by entropic effects,[35] but it is still unfavorable). As discussed above (*cf.*, Tables 1, 2 and 3), the A → B reaction step is exothermic for AS and SS2 mechanisms, whereas it is energy consuming for the SS1 and DIS reaction pathways (by 34 and 42 kJ.mol^{-1}, respectively). The overall energetics of the first half-reaction thus favors the associative mechanism (over the SS1 with the most stable structure **A**), in agreement with our previous vacuum calculations.[35] The electron transfer in the SS1 mechanism is also expected to be less probable, due to the larger manganese–superoxide separation.

4.2. Second half-reaction: reduction of $O_2^{\bullet-}$ to O_2^{2-} coupled with proton transfer. In this section, we compare the four different mechanisms for the second half-reaction (dissociative, associative and the two second-sphere, SS1 and SS2). In order to compare the energies of the **C** structure, the molecular and solvation energy of one water molecule optimized in water-like environment ($\varepsilon_r = 80$) must be added to energies of relevant structures in dissociative mechanism in order to compare them with the other two mechanisms (in the same way as for the first half-reaction).

Xxx No paragraph break. The four relevant structures - are depicted in Figure 8. A comparison of the QM/MM energies or estimates of the Gibbs free energies for these four structures show that the SS2 structure is preferred (Figure 8). The SS1, AS and DIS complexes are 30, 34 and 40 kJ.mol^{-1} less stable.

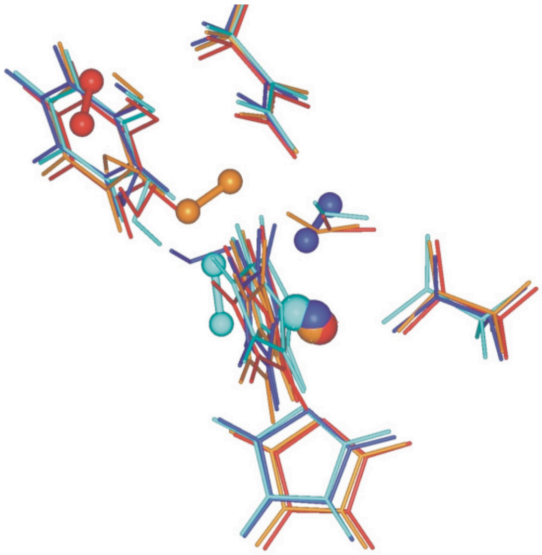

Structure	S	$\Delta E_{QM/MM}$	ΔG
AS	3	43.5	33.9
SS1	3	29.8	29.8
SS2	3	0.0	0.0
DIS	3	94.6	82.9

Figure 8. A superimposition of the active sites of the most stable Mn^{II}-$O_2^{\bullet-}$ structures: $\mathbf{C_{as}}$, $\mathbf{C_{SS1/SS2}}$ (depicted in Figures 2 and 4) and $\mathbf{C_{dis}}$ in septet spin state. The AS, SS1, SS2 and DIS geometries are drawn in red, green, orange and blue color, respectively. Their relative QM(B3LYP/TZP)/MM energies, $\Delta E_{QM/MM}$, and estimated Gibbs free energy ΔG are shown as well. All energies are in kJ.mol^{-1}. **Xxx For ΔG DIS, you should add the transaltional and rotational entropy of a free H2O molecule, ~55 kJ/mol.**

These relative energies of the reactant state for the various mechanisms can be combined with the energies for the putative reaction intermediates discussed above. We have seen (Tables 2 and 3) that both the $AS_{RED}1$ and SS1 mechanisms involve rather complicated proton transfers via Gln146 and Tyr34 and that possible intermediates along this proton-transfer path are high inenergy (90–141 kJ.mol^{-1}). On the other hand, the proton transfers in the SS2 and $AS_{RED}2$ mechanisms are simple and have estimated barriers of 62–67 kJ.mol^{-1} and 21 kJ.mol^{-1}, respectively. Although there is a lower activation barrier in

$AS_{RED}2$ than SS2 mechanism, the higher stability of the SS2 reactant ($\mathbf{C_{SS2}}$) compensates the kinetic preference of $AS_{RED}2$. **Xxx Is it really so? 21+34=55 kJ, which is lower than 62-67. So if we use the DG value, the AS path is actually preferable, and even with the EQM/MM value (21+44=65), the two mechanism get a similar energy.** Moreover, the entropy effect can be expected to favor SS2 over $AS_{RED}2$ mechanism. Thus, our results indicate that the SS2 mechanism is most likely. Again, this is in agreement with the QM studies on small vacuum models of MnSOD.[11]

5. Conclusions

In this work, we attempted to address the reaction mechanism of manganese super oxide dismutase by QM/MM calculations, which were followed by the reference CASSCF/CASPT2 calculations on the most interesting structures. The presented work complements our previous two studies carried out using a small first-sphere model of MnSOD[35] and the quantum refinement (QM/MM/X-ray) study on resting form of MnSOD.[11] It provides a rigorous theoretical footing for the discussions of different reaction pathways (dissociative, associative, and second sphere), which were, up to date, based on the indirect experimental evidence or the calculations on the small models of the active site. Our results suggest that the first half-reaction ($O_2^{\bullet-}$ to O_2 oxidation) is likely to follow an associative reaction pathway (superoxide binds as the sixth ligand to the manganese center), whereas the second half-reaction ($O_2^{\bullet-}$ to O_2^{2-} reduction) proceeds via a second-sphere mechanism in which the substrate binds to the Mn-bound solvent molecule. However, the associative pathway, involving a direct ($H_2O_{Mn\text{-}bound} \rightarrow O_2^{\bullet-}$) proton transfer, denoted $AS_{RED}2$, can represent a competitive mechanism for the second half-reaction. The calculated reaction barriers (obtained using both B3LYP density functional and CASSCF/CASPT2 methods and appearing as the crossing of the two potential energy surfaces of different multiplicity) are in resonable agreement with the enzyme's catalytic turnover. Therefore, we consider the presented results as an important theoretical contribution, extending our understanding of this biochemically and medicinally interesting system.

Acknowledgment We gratefully acknowledge financial support by the Ministry of Education, Youth, and Sports of the Czech Republic (research projects Z40550506 and LC512) and by the Swedish research council (UR) and the computer resources of Lunarc at Lund University.

Supporting Information Available. The protein coordinates and the point charges on all atoms in MM region (in PDB format) and the equilibrium geometries of the quantum region for all of the studied structures are available free of charge via WWW on http:/pubs.acs.org.

References

(1) Miller, A.-F.; Sorkin, D. L. *Comments Mol. Cell Biophys.* **1997**, *9*, 1-48.

(2) Miller, A.-F. In Handbook of Metalloproteins, Messerschmidt A, Huber R, Wieghardt K, Poulos T, Eds, John Wiley & Sons: Chichester (2001) pp. 668-692.

(3) Stroupe, M. E.; DiDonato, M.; Tainer, J.A. In Handbook of Metalloproteins, Messerschmidt A, Huber R, Wieghardt K, Poulos T, Eds, John Wiley & Sons: Chichester (2001) pp. 941-951.

(4) Bordo, D.; Pesce, A.; Bolognesi, M.; Stroppolo, M. E.; Falconi, M.; Desideri, A. In Handbook of Metalloproteins, Messerschmidt A, Huber R, Wieghardt K, Poulos T, Eds, John Wiley & Sons: Chichester (2001) pp. 1284-1300.

(5) Wuerges, J.; Lee, J.-W.; Yim, Y.-I.; Yim, H.-S.; Kang, S.-O.; Carugo, K. D. *Proc Natl. Acad. Sci. U.S.A.* **2004**, *101*, 8569-8574.

(6) Getzoff, E. D.; Tainer, J. A; Stempien, M. M.; Bell, G. I.; Hallewell, R. A. *Proteins Struct. Funct. Genet.* **1989**, *5*, 322-336.

(7) Steinman, H. M.; Weinstein, L.; Brenowitz, M. *J. Biol. Chem.* **1994**, *269*, 28629-28634.

(8) Chance, B.; Sies, H.; Boveris, A. *Physiol. Rev.* **1979**, *59*, 527-605.

(9) Bull, C.; Niederhoffer, E. C.; Yoshida, T.; Fee, J. A. *J. Am. Chem. Soc.* **1991**, *113*, 4069-4076.

(10) B. F. Anderson, R. A. Edwards, M. M. Whittaker, J. W. Whittaker, E. N. Baker, G. B. Jameson, *to be published*; PDB files 1ix9 and 1ixb.

(11) Rulíšek, L.; Ryde, U. *J. Phys. Chem.* B **2006**, *110*, 11511-11518.

(12) Stallings, W. C.; Metzger, A. L.; Pattridge, K. A.; Fee, J. A.; Ludwig, M. L. *Free Rad. Res. Commun.* **1991**, *12-13*, 259-268.

(13) Han, W.-G.; Lovell, T.; Noodleman L. *Inorg. Chem.* **2002**, *41*, 205-218.

(14) Hunter, T.; Ikebukuro, K.; Bannister, W. H.; Bannister, J. V; Hunter, G. J. *Biochemistry* **1997**, *36*, 4925-4933.

(15) Jackson, T.A.; Brunold, T. C. *Acc. Chem. Res.* **2004**, *37*, 461-470.

(16) Hsieh, Y.; Guan, Y.; Tu, C.; Bratt, P. J.; Angerhofer, A.; Lepock, J. R.; Hickey, M. J.; Tainer, J. A.; Nick, H. S.; Silverman, D. N. *Biochemistry* **1998**, *37*, 4731-4739.

(17) Yikilmaz, E.; Xie, J.; Brunold, T. C.; Miller, A.-F. *J. Am. Chem. Soc.* **2002**, *124*, 3482-3483.

(18) Whittaker, M. M.; Whittaker, J. W. *Biochemistry* **1997**, *36*, 8923-8931.

(19) Guan, Y.; Hickey, M. J.; Borgstahl, G. E. O.; Hallewell, R. A.; Lepock, J. R.; O'Connor, D.; Hsieh, Y.; Nick, H. S.; Silverman, D. N.; Tainer, J. A. *Biochemistry* **1998**, *37*, 4722-4730.

(20) Riley, D. P. *Chem. Rev.* **1999**, *99*, 2573-2587.

(21) Sayre, L. M.; Perry, G.; Smith, M. A. *Curr. Opin. Chem. Biol.* **1999**, *3*, 220-225.

(22) McCord, J. M. *Methods in Enzymol.* **2002**, *349*, 331-341.

(23) Hsu, J. L.; Hsieh, Y.; Tu, C.; O'Connor, D.; Nick, H. S.; Silverman, A. N. *J. Biol. Chem.* **1996**, *271*, 17687-17691.

(24) Lah, M. S.; Dixon, M. M.; Pattridge, K. A.; Stallings, W. C.; Fee, J. A.; Ludwig, M. L. *Biochemistry* **1995**, *34*, 1646-1660.

(25) Jackson, T.A.; Yikilmaz, E.; Miller, A.-F.; Brunold, T. C. *J. Am. Chem. Soc.* **2003**, *125*, 8348-8363.

(26) Whittaker, J. W.; Solomon, E. I. *J. Am. Chem. Soc.* **1988**, *110*, 5329-5339.

(27) Vatyam, S.; Byrd, R. A.; Miller, A.-F. *Magn. Reson. Chem.* **2000**, *38*, 536-542.

(28) Whittaker, M. M.; Ekberg, C. A.; Edwards, R. A.; Baker, E. N.; Jameson, G. B.; Whittaker, J. W. *J. Phys. Chem. B* **1998**, *102*, 4668-4677.

(29) Yikilmaz, E.; Xie, J.; Brunold, T. C.; Miller, A.-F. *J. Am. Chem. Soc.* **2002**, *124*, 3482-3483.

(30) Xie, J.; Yikilmaz, E.; Miller, A.-F.; Brunold, T. C. *J. Am. Chem. Soc.* **2002**, *124*, 3769-3774.

(31) Jackson, T.A.; Xie, J.; Yikilmaz, E.; Miller, A.-F.; Brunold, T. C. *J. Am. Chem. Soc.* **2002**, *124*, 10833-10845.

(32) Jackson, T.A.; Karaetia, A..; Miller, A.-F.; Brunold, T. C. *J. Am. Chem. Soc.* **2004**, *126*, 12477-12491.

(33) Fisher, C. L.; Chen, J.-L.; Li, J; Bashford, D.; Noodleman, L. *J. Phys. Chem.* **1996**, *100*, 13498-13505.

(34) Li, J; Fisher, C. L.; Konecny, R.; Bashford, D.; Noodleman, L. *Inorg. Chem.* **1999**, *38*, 929-939.

(35) Rulíšek, L.; Jensen, K. P.; Lundgren, K.; Ryde, U. *J. Comput. Chem.* **2006**, *27*, 1398-1414.

(36) Ryde, U. *J. Comput.-Aided Mol. Design* **1996**, *10*, 153-164.

(37) Ryde, U.; Olsson, M. H. M. *Int. J. Quantum Chem.* **2001**, *81*, 335-347.

(38) Treutler, O.; Ahlrichs, R. *J. Chem. Phys.* **1995**, *102*, 346-354.

(39) Case, D. A.; Pearlman, D. A.; Caldwell, J. W.; Cheatham III, T. E.; Wang, J.; Ross, W. S.; Simmerling, C. L.; Darden, T. A.; Merz, K. M.; Stanton, R. V.; Cheng, A. L.; Vincent, J. J.; Crowley, M.; Tsui, V.; Gohlke, H.; Radmer, R. J.; Duan, Y.; Pitera, J.; Massova, I.; Seibel, G. L.; Singh, U. C.; Werner, PI. K.; Kolman, PI.. A. AMBER 7, University of California, San Francisco, 2002.

(40) Cornell, W. D.; Cieplak, PI.; Bayly, C. I.; Gould, I. R.; Merz, K. M.; Ferguson, D. M.; Spellmeyer, D. C.; Fox, T.; Caldwell, J. W.; Kolman, PI.. A. *J. Am. Chem. Soc.* **1995**, *117*, 5179-5197.

(41) Reuter, NI.; Dejaegere, A.; Maigret, B.; Karplus, M. *J. Phys. Chem.* **2000**, *104*, 1720-1735.

(42) Svensson, M.; Humbel, S.; Froese, R. D. J.; Matsubara, T.; Sieber, S.; Morokuma, K. *J. Phys. Chem.* **1996**, *100*, 19357-19363.

(43) Sigfridsson, E.; Ryde, U. *J. Comput. Chem.* **1998**, *19*, 377-395.

(44) Ahlrichs, R.; Bär, M.; Häser, M.; Horn, H.; Kölmel, C. *Chem. Phys. Lett.* **1989** *162*, 165-169.

(45) Perdew, J. P.; Burke, K.; Ernzerhof, M. *Phys. Rev. Lett.*, **1996**, *77*, 3865-3868.

(46) (a) A. D. Becke, *Phys. Rev. A* **1988**, *38*, 3098-3100. (b) C. T. Lee, W. T. Yang, R. G. Parr, *Phys. Rev. B* **1988**, *37*, 785-789. (c) A. D. Becke, *J. Chem. Phys.* **1993**, *98*, 5648-5652.

(47) Eichkorn, K.; Treutler, O.; Öhm, H.; Häser, M.; Ahlrichs, R. *Chem. Phys. Lett.* **1995**, *240*, 283-290.

(48) Eichkorn, K.; Weigen, F.; Treutler, O.; Ahlrichs, R. *Theor. Chim. Acta* **1997**, *97*, 119-124.

(49) Hehre, W. J.; Radom, L.; Schleyer, PI. v. R.; Pople, J. A. *Ab initio molecular orbital theory*; Wiley-Interscience: New York, 1986.

(50) Schäfer, A.; Huber, C.; Ahlrichs, R. *J. Chem. Phys.* **1994**, *100*, 5829-5835.

(52) Wachters, A. J. *J. Chem. Phys.* **1970**, *52*, 1033-1036. (b) Hay, P. J. *J. Chem. Phys.* **1977**, *66*, 4377-4384.

(53) Jensen, F. *Introduction to Computational Chemistry*; John Wiley & Sons, 1999.

(54) Noodleman, L. *J. Chem. Phys.* **1981**, *74*, 5737-5743.

(55) Neese F. ORCA, *An ab initio, Density Functional, and Semiempirical Program Package*, University of Bonn, Bonn, Germany, 2007.

(56) Roos, B. O.; Taylor, P. R. Chem. Phys. 1980, 48, 157-173.

(57) Andersson, K.; Malmqvist, P.-Å.; Roos, B. O. J. Chem. Phys. 1992, 96, 1218-1226.

(58) Karlström, G.; Lindh, R.; Malmqvist, P.-Å.; Roos, B. O.; Ryde, U.; Veryazov, V.; Widmark, P.-O.; Cossi, M.; Schimmelpfennig, B.; Neogrady, P.; Seijo, L. Comp. Mater. Sci. 2003, 28, 222-239.

(59) Pierloot K.; Dumez B.; Widmark P.-O.; Roos B. O. *Theor. Chim. Acta* **1995**, *90*, 87-114.

(60) (a) Aquilante, F.; Pedersen, T. B.; Lindh, R. *J. Chem. Phys.* **2007**, *126*, 194106-194111. (b) Aquilante, F.; Malmqvist, P.-Å.; Pedersen, T. B.; Ghosh, A.; Roos, B. O. *J. Chem. Theory Comp.* **2008**, *4*, 694-702. (c) Aquilante, F.; Pedersen, T. B.; Sanchez de Meras, A.; Koch, H.; Lindh, R.; Roos, B. O. *J. Chem. Phys.* **2008**, *129*, 24113-24118.

(61) (a) Roos, B. O.; Andersson, K. Chem. Phys. Lett. 1995, 245, 215-243. (b) Forsberg, N.; Malmqvist, P.-Å. Chem. Phys. Lett. 1997, 274, 196-204.

(62) Berendsen, H. J. C.; Postma, J. P. M.; van Gunsteren, W. F.; DiNola, A.; Haak, J. R. *J. Chem. Phys*. **1984**, *81*, 3684-3690.

(63) Siegbahn, P. E. M.; Blomberg, M. R. A. *Chem. Rev*. **2000**, *100*, 421-437.

(64) Blomberg, M. R. A.; Siegbahn, P. E. M. *Theor. Chem. Acc*. **1997**, *97*, 72-80.

(65) Hearn A. S.; Stroupe M.E.; Cabelli D.E.; Lepock J. R.; Tainer J. A.; Nick H. S.; Silverman D. N. *Biochemistry* **2001**, 40, 12051-12058.

(66) Carraso R.; Morgenstern-Badarau I.; Cano J. *Inorg Chim Acta* **2007**, 360, 91-101.

(67) Gray, H. B; Winkler, J. R. *Proc. Natl. Acad. Sci. U. S. A.* **2005**, *102*, 3534-3539.

(68) Ren X.; Tu C.; Bhatt D.; Perry J. J. P.; Tainer J. A.; Cabelli D. E.; Silverman D. N. *J. Mol. Structure* **2006**, *1-3*, 168-173.

SYNOPSIS TOC